INORGANIC CHEMISTRY FRONTIERS

RESEARCH ARTICLE

View Article Online
View Journal | View Issue

Check for updates

Cite this: *Inorg. Chem. Front.*, 2024, **11**, 4439

GSH/pH dual-activated POM@MOF for tumor cell-specific synergistic photothermal and chemodynamic therapy†

Bole Li,‡[a] Zhujun Wu,‡[b] Xiaotong Xu,[a] Yanfei Lv,[a] Yunfei Guo,[a] Siyu Liang,[a] Zhimin Wang,*[b] Lei He *[a] and Yu-Fei Song *[a]

Received 30th April 2024,
Accepted 11th June 2024

DOI: 10.1039/d4qi01079e

rsc.li/frontiers-inorganic

Published on 11 Khotavuxika 2024. Downloaded on 2026-02-17 05:35:50.

Photothermal therapy (PTT) is emerging as a promising therapeutic approach for tumor treatment. However, the low therapeutic effect of photothermal agents due to their non-specificity and the monotherapy approach remains challenging for further applications. Herein, tumor microenvironment (TME) specifically responsive POM@MOF composites with sequential activation properties were constructed by encapsulating POMs (PMo_{12}, short for $H_3PMo_{12}O_{40}$) into metal organic framework (MIL-101) carriers for synergistic PTT/chemodynamic therapy (CDT) treatment. PMo_{12}@MIL-101 releases PMo_{12} and Fe^{3+} under acidic TME conditions, which are subsequently converted into reduced PMo_{12} and Fe^{2+} by GSH in the TME. PMo_{12} in its reduced state exhibits excellent photothermal conversion efficiency (47.03%) under near-infrared laser irradiation, which boosts the CDT effects by accelerating the reaction between H_2O_2 and Fe^{2+} and producing more $^{\bullet}OH$ radicals. The resulting PTT/CDT synergistic therapeutic effects are highly dependent on the pH value and GSH concentration in the TME, and exhibit a strong inhibition of HepG2 cell proliferation compared to monotherapy.

Introduction

Photothermal therapy (PTT) is an emerging cancer treatment that uses a photothermal agent (PTA) to convert near-infrared (NIR) light into heat for tumor ablation.[1] Due to the minimal invasiveness and precise spatial specificity, PTT has been recognized as an effective strategy for cancer treatment and has attracted extensive attention in recent years.[2,3] Many PTAs, including inorganic nanomaterials (*e.g.*, black phosphorus nanosheets and Au nanorods),[4,5] organic molecules (*e.g.*, ICG),[6–9] and polymeric materials (*e.g.*, polydopamine),[10,11] have been developed for cancer treatments. However, the practical application of PTAs in cancer treatment remains challenging due to two main reasons: (a) most PTAs are non-specific and randomly distributed throughout the body, requiring manual intervention to achieve targeted therapy, which demands a high level of manipulation; (b) PTT alone is insufficient in eradicating tumors due to the inhomogeneous heat distribution throughout the tumor tissue, resulting in inevitable tumor recurrence and metastasis.[12,13] Therefore, it is crucial to develop tumor cell-specific PTAs and to integrate them with other therapeutic strategies.

Polyoxometalates (POMs) are a class of nanoscale inorganic polymetallic oxygen clusters that have a wide range of applications in catalysis, assembly, and biomedicine.[14–17] Recently, POMs have shown great potential in biomedical research fields due to their high biocompatibility, versatile structures, adjustable compositions, low cost and easy availability.[18,19] Particularly, the reduction of Mo-based POMs to molybdenum blue produces strong absorption in the NIR region, giving Mo-based POMs great potential as PTAs.[20–22] In addition, POMs have exhibited acid-activated self-assembly properties that enhance the retention by self-assembling into aggregates once they enter the acidic tumor microenvironment (TME).[23–25] These characteristics endow POMs with a tumor cell-specific activation property as PTAs. Nevertheless, the highly negatively charged surface of POMs makes it difficult to cross cell membranes,[26–28] and thus carriers are often used to enhance the cellular uptake of POMs.

Metal organic frameworks (MOFs) are considered as a promising class of drug carriers due to their well-defined structure, tunable pore size, pH-responsiveness, and biodegradability.[29,30] A variety of POM@MOF materials have been reported in recent years, and the corresponding preparation approaches are well-established.[17,31] POMs residing in

[a]*State Key Laboratory of Chemical Resource Engineering, Beijing University of Chemical Technology, Beijing 100029, P. R. China. E-mail: helei@mail.buct.edu.cn, songyf@mail.buct.edu.cn; Fax: +86-10-64431832; Tel: +86-10-64431832*
[b]*Advanced Research Institute of Multidisciplinary Science, Beijing Institute of Technology, Beijing, 100081, P. R. China. E-mail: zmwang@bit.edu.cn*
†Electronic supplementary information (ESI) available. See DOI: https://doi.org/10.1039/d4qi01079e
‡These authors contributed equally.

Published on 11 Khotavuxika 2024. Downloaded on 2026-02-17 05:35:50.

the MOF cavity avoid the ineffective encapsulation caused by the surface loading, and maintain a high stability of the POM structure.[32] Notably, MOFs have adjustable inorganic metal centers, which endow them with intrinsic Fenton catalytic activity as a chemodynamic therapy (CDT) agent by tuning the metal center such as Fe and Cu.[33,34] As such, the encapsulation of POMs into MOFs will not only enhance cellular uptake efficacy by improving the surface charges of POMs, but also endow them with tumor cell-specifically activated PTT/CDT combined therapeutic effects.

In this work, we report a TME-responsive POM@MOF (PMo_{12}@MIL-101, denoted as P@M) therapeutic agent with sequential activation properties for synergistic PTT/CDT therapy (Fig. 1). By confining PMo_{12} with activated photothermal conversion properties to MIL-101, the low cellular uptake efficacy of PMo_{12} that is caused by its highly negative surface charge can be avoided. The MIL-101 structure collapses in the acidic and reducing TME, favoring the activated release of PMo_{12} in tumor cells. The released PMo_{12} is reduced and aggregated under endogenous GSH and acidic conditions, resulting in electron transfer and a subsequent photothermal effect that triggers thermal ablation of tumor cells under NIR laser irradiation (808 nm). Concurrently, the released Fe^{3+} is reduced to Fe^{2+} by GSH, which further causes massive generation of $^{\bullet}OH$ from overexpressed H_2O_2 in the TME *via* the Fenton reaction. In addition, local hyperthermia promotes the Fenton reaction and enhances the effect of CDT, and thus the synergistic effect of combined PTT/CDT therapy shows excellent efficacy in suppressing tumor cell proliferation.

Results and discussion

As shown in Fig. 2A, P@M was synthesized *via* the one-pot solvothermal method.[35] Scanning electron microscopy (SEM) images showed that P@M resembled MIL-101 in the monodisperse octahedral morphology, with a size of approximately 800 nm (Fig. 2B and S1†), suggesting that the morphology of MIL-101 remained unchanged upon encapsulation of PMo_{12}. No obvious small particles were observed on the surface of the octahedral structure, which indicated that PMo_{12} was orderly assembled with MIL-101 rather than being self-assembled and then composited with MIL-101. Elemental mapping results displayed that the Mo, Fe, and C elements were uniformly distributed over the entire P@M (Fig. 2C). In addition, the X-ray powder diffraction (XRD) pattern (Fig. S2†) of P@M closely resembled that of MIL-101,[36] providing additional evidence that the framework of MIL-101 was not affected by PMo_{12}. Note that no obvious XRD patterns attributable to PMo_{12} were detected in P@M, which further demonstrated that PMo_{12} clusters were well dispersed without aggregation. The content of PMo_{12} in P@M was calculated to be 26.8% from the ICP results (Table S1†). Moreover, as shown in Fig. 2D, PMo_{12} alone exhibited a negative zeta potential because of the highly

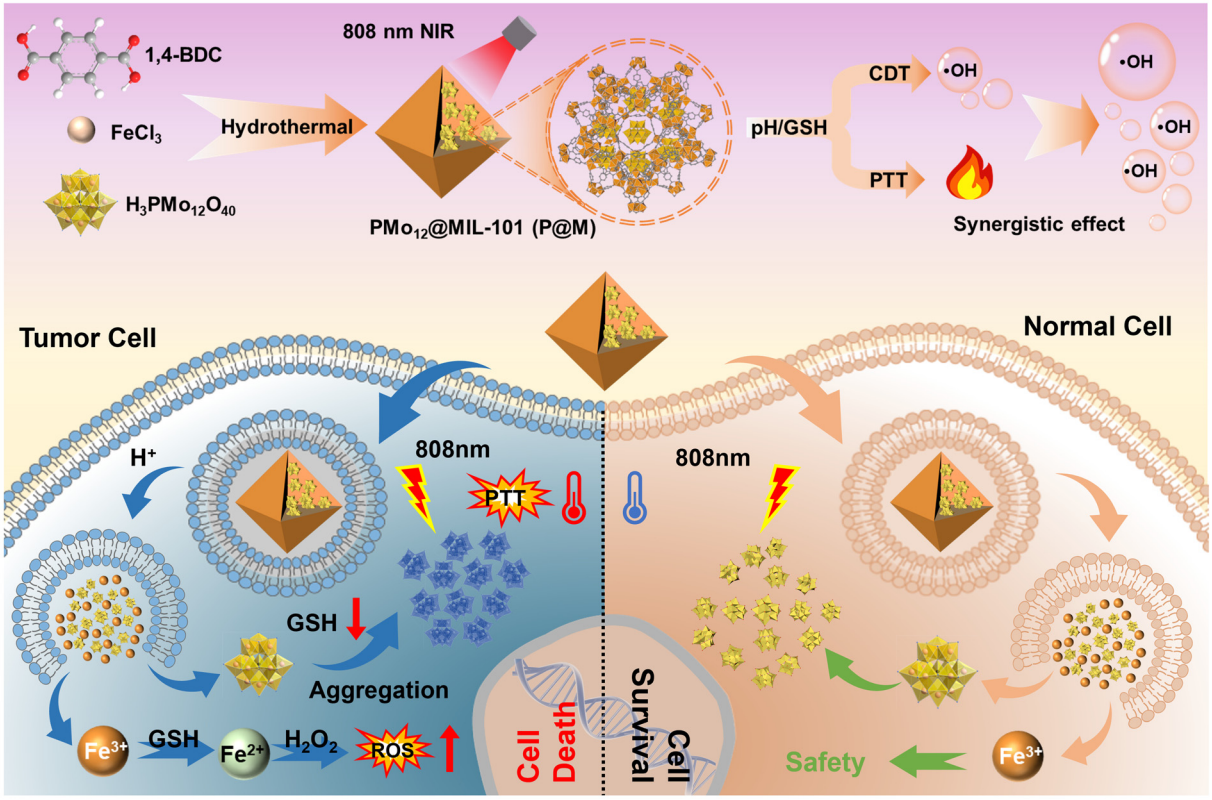

Fig. 1 Schematic illustration of tumor cell-specific GSH/pH dual activated P@M for combined PTT/CDT treatment.

 This journal is © the Partner Organisations 2024

Published on 11 Khotavuxika 2024. Downloaded on 2026-02-17 05:35:50.

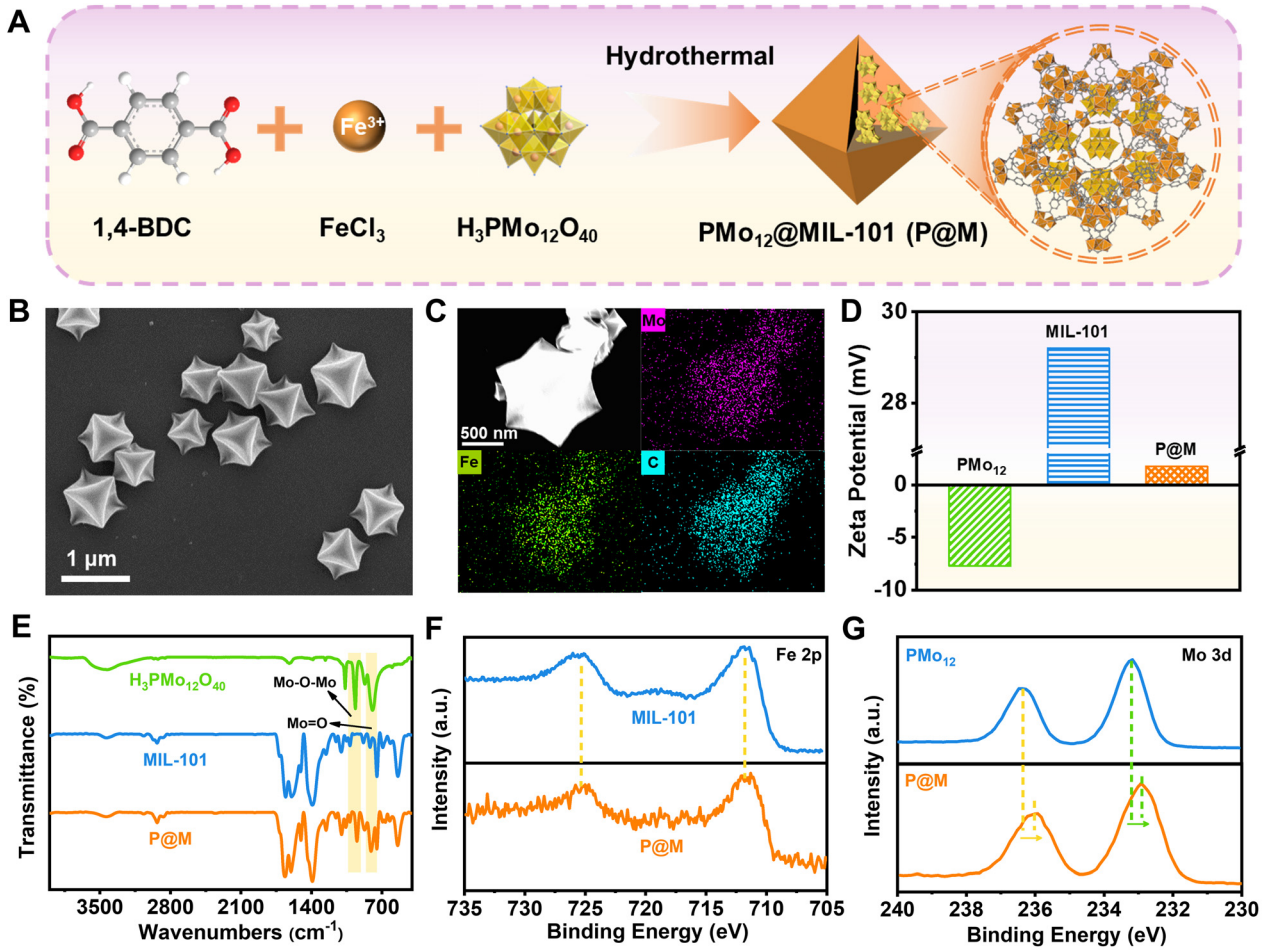

Fig. 2 Preparation and characterization of P@M. (A) Schematic illustration of the synthetic route for P@M. (B) SEM image of P@M. (C) Elemental mappings of Mo, Fe, and C signals. (D) Zeta potential of PMo_{12}, MIL-101 and P@M. (E) FT-IR spectra of PMo_{12}, MIL-101 and P@M. High-resolution XPS spectra of (F) Fe 2p and (G) Mo 3d for PMo_{12} and P@M.

negatively charged surface of the clusters. In contrast, MIL-101 showed a positive zeta potential.[37] The as-prepared P@M exhibited a slightly positive zeta potential, suggesting that PMo_{12} was confined within the MIL-101 cages.

The Fourier transform infrared (FT-IR) spectrum of P@M showed the characteristic bands of both PMo_{12} and MIL-101 (Fig. 2E). The bands at about 542, 749, 1390 and 1598 cm^{-1} were attributed to ν(Fe–O), ν(C–H), ν_s(COO–) and ν_{as}(COO–) of MIL-101, respectively.[38] The four bands at ~1064, 967, 870 and 794 cm^{-1} corresponded to the ν(P–O) of the PO_4 tetrahedron and ν(Mo═O), ν(Mo–O_b–Mo) and ν(Mo–O_e–Mo) of the PMo_{12} cluster, respectively.[39,40] This result indicated that the structure of PMo_{12} was maintained during the encapsulation process. Additionally, the composition and elemental valence of P@M were investigated by X-ray photoelectron spectroscopy (XPS) measurements. For both MIL-101 and P@M, the high-resolution spectrum of Fe 2p exhibited two broad peaks at 711.74 and 725.35 eV, corresponding to Fe^{3+} $2p_{3/2}$ and Fe^{3+} $2p_{1/2}$, respectively (Fig. 2F).[41] The Mo 3d peaks for PMo_{12} located at ~233.2 and 236.3 eV were assigned to Mo^{6+} $3d_{5/2}$ and Mo^{6+} $3d_{3/2}$, respectively (Fig. 2G).[42] Compared with the individual PMo_{12}, the two Mo 3d peaks of P@M shifted slightly toward lower binding energies at ~232.9 and 236.0 eV, which was consistent with those reported in the literature.[35] The results indicated a charge transfer between the MOF and the encapsulated POM, which was attributed to the host–guest interaction.

P@M exhibited a slightly positive zeta potential in phosphate buffer solution (PBS) at pH 7.4 since PMo_{12} was encapsulated in MIL-101 cages (Fig. 3A and B). Intriguingly, the surface potential of P@M became negative in PBS at pH = 5.5, indicating the collapse of the MIL-101 structure and the release of negatively charged POM clusters under acidic conditions. The pH-sensitive property of P@M will make it responsive to the acidic tumor microenvironment. Similar to the individual PMo_{12} clusters (Fig. S3†), P@M showed a strong absorbance in the near-infrared-I (NIR-I) window upon reduction by glutathione (GSH) (Fig. 3C). The absorbance intensity of P@M in its reduced form (denoted as rP@M) increased with an increase in the concentration of GSH. The XPS results (Fig. 3D)

Published on 11 Khotavuxika 2024. Downloaded on 2026-02-17 05:35:50.

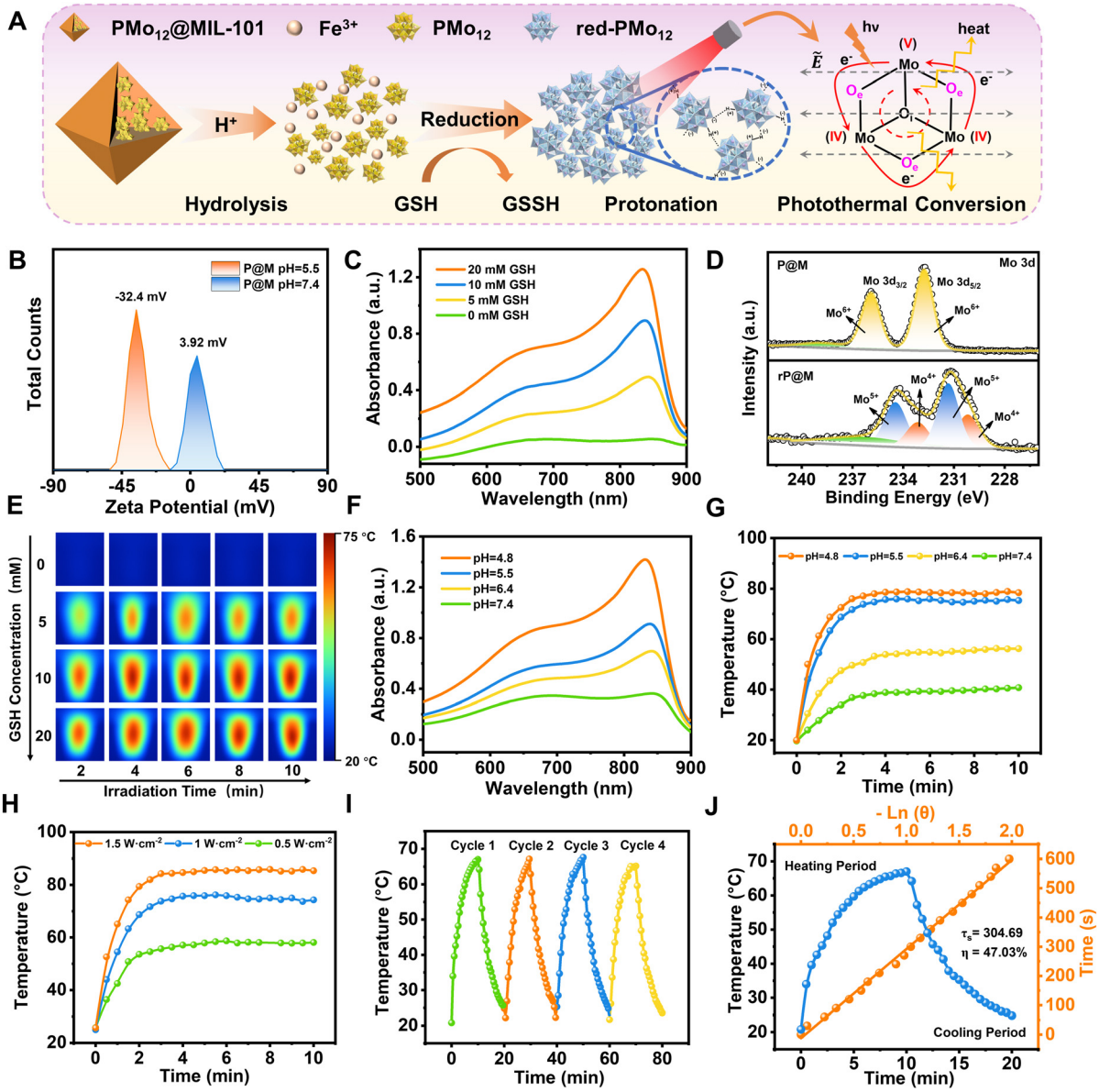

Fig. 3 The activated photothermal conversion performance of P@M. (A) Schematic diagram of the photothermal therapy mechanism of P@M. (B) Zeta potential of P@M in PBS buffer at different pH values. (C) UV-vis spectra of 1 mg mL^{-1} P@M at different GSH concentrations in pH 5.5 buffer. (D) XPS profiles of Mo 3d for P@M and rP@M. (E) Visualized IR thermograms of 1 mg mL^{-1} P@M solutions at different GSH concentrations (0–20 mM) irradiated with an 808 nm laser (1.0 W cm^{-2}) for 10 min. (F) UV-vis spectra of 1 mg mL^{-1} P@M at different pH values in the presence of 10 mM GSH. (G) Temperature changes of 1 mg mL^{-1} P@M solution at different pH values during 10 min of irradiation at 808 nm (1.0 W cm^{-2}) when the GSH concentration is 10 mM. (H) Temperature profiles for 1 mg mL^{-1} P@M under 808 nm laser irradiation at different power densities when the pH value is 5.5 and GSH concentration is 10 mM. (I) Thermal stability of 1 mg mL^{-1} P@M under 808 nm laser irradiation in the presence of 10 mM GSH. (J) Heating and cooling curves of P@M and fitted linear data obtained from the cooling process.

indicated that GSH reduced the Mo in the POM from the oxidation state of Mo(VI) to mixed valence states of Mo(V) and Mo (IV). As illustrated in Fig. 3A, the inter-valence charge transfer between Mo(V) and Mo(IV) *via* the oxo-bridge endowed the reduced P@M with NIR photothermal conversion behaviour.[20,43] As shown in Fig. S4,† a prominent photothermal conversion phenomenon was observed for P@M upon treatment with GSH in PBS (pH = 5.5). The photothermal behavior was found to correlate with the reducibility of Mo over a certain range of GSH concentrations. Visualized IR thermograms showed that the highest solution temperature of P@M could reach about 76 °C when 10 mM GSH was applied to reduce Mo (Fig. 3E and S4†).

In addition, like other Mo-based POMs that are reported in the literature, the individual PMo_{12} was reduced and self-assembled into larger-sized aggregates with a concomitant increase in the number of Mo at mixed-valence states under acidic conditions, which promoted reversible multistep elec-

 This journal is © the Partner Organisations 2024

Published on 11 Khotavuxika 2024. Downloaded on 2026-02-17 05:35:50.

tron exchange and enhanced the electronic relaxation polarization under an applied electric field (laser), leading to an increased NIR absorbance (Fig. S5†).[44,45] As such, for P@M, the acidic solution conditions can not only destruct the MIL-101 framework and release the encapsulated PMo_{12}, but also promote the self-assembly of reduced PMo_{12} and improve the NIR photothermal conversion. As shown in Fig. 3F, the absorption of P@M in the NIR-I window was significantly enhanced with decreasing pH in the presence of GSH (10 mM), confirming the low-pH-induced aggregation property of PMo_{12}. Correspondingly, the temperature of the P@M system with a concentration of 1000 μg mL^{-1} significantly increased with decreasing pH under laser irradiation at 808 nm (1 W cm^{-2}), and the temperature could be elevated to more than 70 °C within 2 min at pH 5.5 (Fig. 3G and S6†). It should be noted that P@M showed no obvious temperature change under 808 nm laser irradiation in the absence of GSH under neutral pH conditions, reflecting that P@M had a pH/GSH dual-activated photothermal conversion property. Moreover, the photothermal behavior of P@M was irradiation power and concentration dependent (Fig. 3H and S7–S9†). P@M maintained good stability in the 4-cycle laser on/off test and its photothermal conversion efficiency was calculated to be 47.03% (Fig. 3I and J), which was comparable to the performance of recently reported inorganic photothermal materials (Fig. S10†). These experimental results demonstrated that P@M has tumor microenvironment-activated photothermal conversion properties, and is a high-performance photothermal material that can be used for photothermal therapy.

Intriguingly, in addition to PMo_{12}, the destruction of P@M also led to the release of free Fe ions. As illustrated in Fig. 4A, the released Fe ions in their reduced state (Fe^{2+}) were speculated to catalyse a Fenton-like reaction, thus functioning as a chemodynamic therapy (CDT) agent. To verify the potential of P@M as a CDT agent, the change in the Fe valence state after treatment with GSH was firstly investigated by XPS. As shown in Fig. 4B, after GSH treatment, the broad Fe^{3+} peaks in P@M, originally located at 712.4 and 725.9 eV, were significantly shifted to lower binding energies in red-P@M, appearing at 709.3 (Fe^{2+} $2p_{3/2}$) and 722.5 eV (Fe^{2+} $2p_{1/2}$), respectively, which indicated that the released Fe^{3+} could be reduced to Fe^{2+} by GSH. In addition, the reduction of Fe^{3+} in P@M was assessed by a chromogenic reaction using *o*-phenanthroline, which reacted with Fe^{2+} to form a complex with an absorbance centered around 510 nm. As shown in Fig. 4C, in a slightly acidic (pH = 5.5) environment, the absorbance of the Fe–*o*-phenanthroline complex gradually increased with increasing GSH concentration. In contrast, no obvious Fe^{2+} was detected without GSH, revealing that GSH induced the reduction of Fe^{3+} to Fe^{2+}. Besides, an obvious increase in the absorbance of the Fe–*o*-phenanthroline complex was observed with a decline in the pH of the P@M solution (Fig. S11†), which further indicated the pH-dependent Fe release of P@M.

The generated Fe^{2+} can react with H_2O_2 and produce ROS through a Fenton reaction (Fig. 4A),[46,47] which will oxidize 3,3′,5,5′-tetramethylbenzidine (TMB) and lead to a color reaction from colorless to blue. As shown in Fig. 4D and S12,† the absorbance of oxTMB at 650 nm was enhanced with an

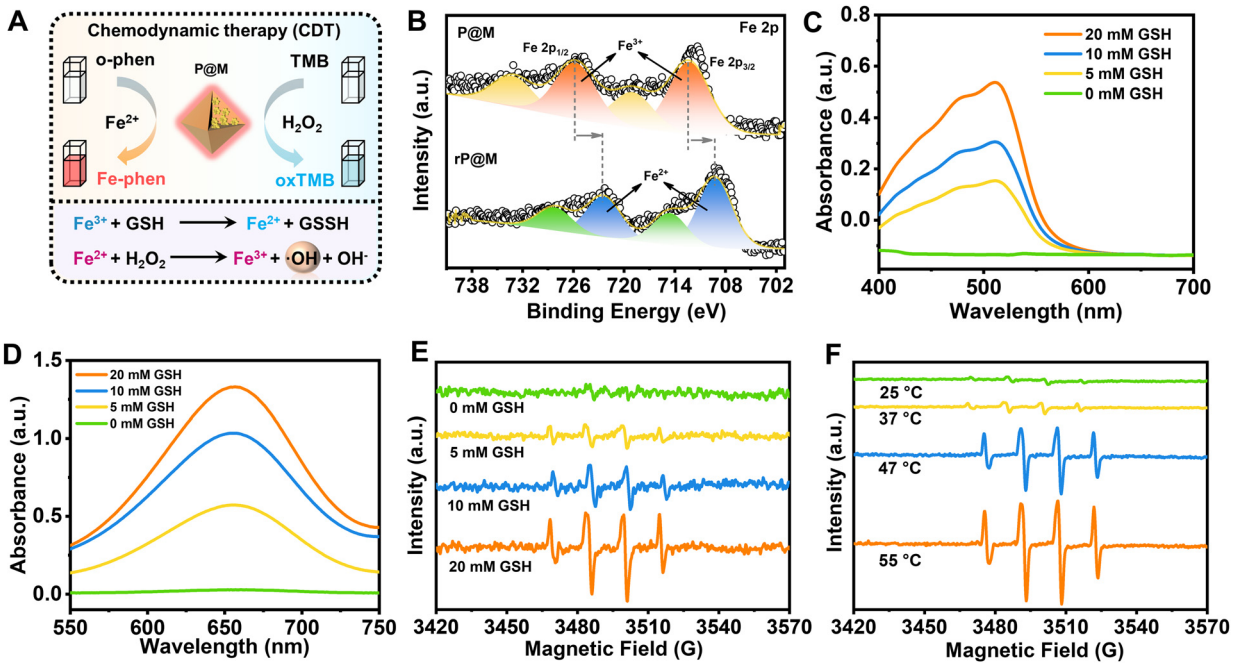

Fig. 4 The activated chemodynamic effect of P@M. (A) Schematic diagram of the mechanism of activated chemodynamic therapy. (B) XPS profiles of Fe 2p for P@M and rP@M. (C) UV-vis spectra of P@M (in PBS, pH 5.5) with *o*-phenanthroline at different GSH concentrations. (D) UV-vis spectra of P@M (in PBS, pH 5.5) with TMB in the presence of 100 μM H_2O_2 at different GSH concentrations. (E) ESR spectra of DMPO/$^{\cdot}$OH for P@M at different GSH concentrations. (F) ESR spectra of DMPO/$^{\cdot}$OH for P@M at different temperatures.

Published on 11 Khotavuxika 2024. Downloaded on 2026-02-17 05:35:50.

increase in GSH concentration or decline in the pH value. The GSH concentration/pH-dependent nature of TMB-related color reaction was consistent with the above-mentioned chromogenic reaction from the complexation of Fe^{2+} and *o*-phenanthroline, which further confirmed the CDT potential of P@M *via* a Fenton reaction. To identify the generated ROS species, an electron spin resonance (ESR) measurement was performed using 5,5-dimethyl-1-pyrroline *N*-oxide (DMPO) as a trapping agent. As shown in Fig. 4E, no signal was detected for P@M without GSH. In contrast, the typical 1 : 2 : 2 : 1 quartet pattern was observed for P@M that reacted with H_2O_2 in the presence of GSH, indicating the generation of the $^{\bullet}OH$ species.

A strengthened ERP signal of $^{\bullet}OH$ was detected with the increase in the concentration of GSH, which proved that the enhanced amount of Fe^{2+} would promote the generation of $^{\bullet}OH$ through a Fenton reaction. The above-mentioned results suggested that P@M had obvious tumor microenvironment-activated Fenton activity and could function as an excellent CDT agent. Interestingly, the production of $^{\bullet}OH$ showed a temperature-dependent behavior. As shown in Fig. 4F, there was a significant increase in $^{\bullet}OH$ production when the temperature rose from 25 to 55 °C, indicating that high temperatures would promote Fenton-like reaction. Notably, the ROS production at body temperature (37 °C) was much lower than that when heated, which ensured the safety of P@M for normal cells or tissues. The results suggested that P@M might have a great synergistic effect by exerting combined PTT and CDT functions.

Encouraged by the prominent photothermal effect and efficient Fenton reaction activity of P@M, its potential therapeutic effect on cancer cells was further investigated. Fig. 5A shows that after a 24 h-incubation with P@M, distinct dark

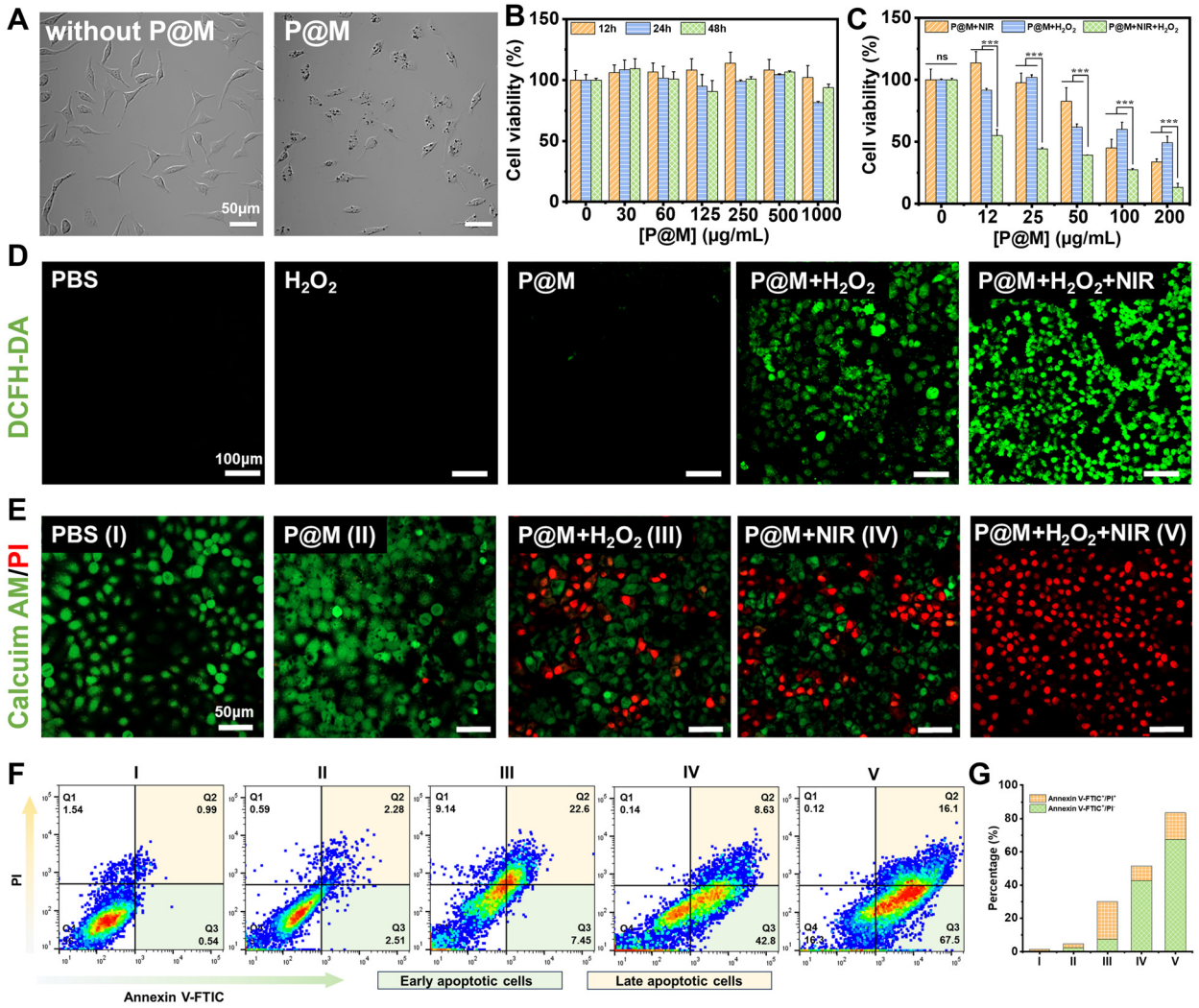

Fig. 5 (A) Cellular uptake of P@M in HepG2 cells. (B) HepG2 cell viabilities after the treatment with different concentrations of P@M for 12, 24 and 48 h. (C) Cytotoxicity assays of HepG2 cells with PTT, CDT and PTT/CDT treatments. Statistical analysis was performed *via* two-way ANOVA with Bonferroni's multiple comparisons test. ***P < 0.001; data are presented as means ± SD (n = 3). (D) CLSM images of intracellular ROS levels with different treatments. (E) Calcein AM/PI double staining of HepG2 cells with different treatments. (F) Flow cytometry analysis of the apoptosis of HepG2 cells subjected to different treatments and (G) corresponding quantitative analysis of cell apoptosis percentages.

 This journal is © the Partner Organisations 2024

Published on 11 Khotavuxika 2024. Downloaded on 2026-02-17 05:35:50.

granules were observed in the cells compared to untreated HepG2 cells, indicating the cellular uptake of P@M. As shown in Fig. 5B, no significant decline in cell viability was observed after treating HepG2 cells with 0–500 μg mL^{-1} P@M for 12, 24, and 48 h. Notably, cell viability remained above 90% even after 48 h of co-culturing with high concentrations of P@M up to 1000 μg mL^{-1}, which indicated that P@M had negligible cytotoxicity against the HepG2 cell line. H_2O_2 alone has no obvious cytotoxicity to HepG2 cells (Fig. S13†).

To assess the therapeutic efficacy of P@M as a PTT and CDT agent, HepG2 cells were exposed to 808 nm laser irradiation (1 W cm^{-2}, 5 min, NIR), H_2O_2 and NIR/H_2O_2 combination in the presence of P@M (Fig. 5C). Cell survival in all the three groups exhibited a predominant dose-dependent trend with P@M. At a concentration of 200 μg mL^{-1}, the cell viability was 34.3% for the P@M + NIR group, 49.8% for the P@M + H_2O_2 group, and 14.8% for the P@M + NIR + H_2O_2 group, respectively. These results demonstrated the potential of P@M for PTT and CDT, as well as its synergistic effect when used in a PTT/CDT-combination therapy.

To investigate P@M-induced intracellular ROS generation, HepG2 cells were stained with 2′,7′-dichlorodihydrofluorescein diacetate (DCFH-DA), a commercially available fluorescent probe, under various treatment conditions (Fig. 5D). Compared to the control group treated with PBS, neither the H_2O_2 nor the P@M treated group showed an increase in ROS levels. In contrast, the P@M + H_2O_2 group showed a remarkable green fluorescence, indicative of an intracellular Fenton reaction with ROS generation. Intriguingly, a significant elevation in ROS levels was observed in the P@M + NIR + H_2O_2 group compared to that of the P@M + H_2O_2 group, which demonstrated that hyperthermia may boost the CDT process.

Calcein-AM/PI double staining was further performed for the direct visualization of cell viability (Fig. 5E). Negligible cell death was observed in both the PBS control and P@M (200 μg mL^{-1}) treatment groups. Notably, CDT (P@M + H_2O_2) and PTT (P@M + NIR) treatments resulted in a substantial increase in cell death, especially in the PTT and CDT co-treated group (P@M + H_2O_2 + NIR), where nearly all cells in the irradiated region were killed. An annexin V-FITC and PI double staining assay was carried out to investigate the ability of P@M to induce cell apoptosis (Fig. 5F). The PTT + CDT combination treatment group (P@M + H_2O_2 + NIR) exhibited the highest efficiency in inducing cell apoptosis, with an apoptotic ratio (sum of Q_2 and Q_3) of 83.6%, evidently higher than the ratios observed in the P@M (4.79%), P@M + H_2O_2 (30.05%) and P@M + NIR (51.43%) groups under identical conditions (Fig. 5G). These results provided compelling evidence that the combination therapy of P@M with PTT and CDT activities was effective in triggering apoptosis compared to therapy with PTT and CDT alone, suggesting a synergistic role for P@M in cancer therapy.

Finally, the potential *in vivo* toxicity of P@M was evaluated. Normal 8-week-old male Balb/c mice were used in the *in vivo* experiments. All animal experiments comply with the Animal Ethical and Welfare Committee of Beijing Institute of Technology. The hematological and histological data were collected and analyzed after intravenous injection with P@M (dose: 20 mg kg^{-1}) into the tails of healthy mice. As shown in Fig. S14,† in routine blood tests, there was no statistically significant difference between the P@M administration group and the control group in the measurement results of white blood cells (WBC), red blood cells (RBC), hemoglobin (HGB), hematocrit (HCT), mean corpuscular volume (MCV), mean corpuscular hemoglobin (MCH) and mean platelet volume (MPV). Moreover, renal function indicators such as blood urea nitrogen (BUN), uric acid (UA) and creatinine (CRE) were comparable to those of the control group. Meanwhile, the corresponding histological changes in the major organs of mice, including the heart, liver, spleen, lungs, and kidneys, harvested after administration were analyzed by typical H&E staining (Fig. 6). The results showed no obvious signs of damage to the normal anatomical structure of the organs. These findings demonstrated the high biocompatibility and biosafety of P@M.

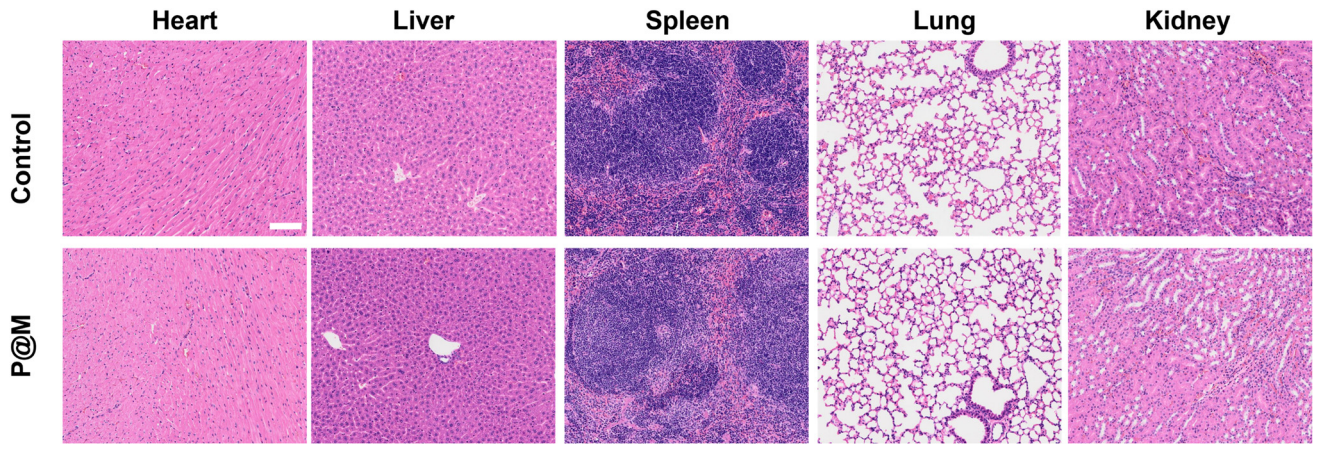

Fig. 6 Histological examinations of major organs of mice after intravenous injection with P@M (scale bar: 100 μm).

Published on 11 Khotavuxika 2024. Downloaded on 2026-02-17 05:35:50.

Conclusions

In conclusion, GSH/pH dual-activated P@M that specifically responds to the TME was successfully developed for synergistic PTT/CDT therapy. Fe^{3+} and PMo_{12} clusters were released from P@M when exposed to relatively acidic conditions, and were subsequently reduced by GSH in the TME. The generated Fe^{2+} showed Fenton-like activity to catalyze the formation of highly toxic $^{\bullet}OH$ from H_2O_2, while the reduced PMo_{12} clusters displayed an excellent photothermal conversion efficiency as high as 47.03% under NIR irradiation. Both ESR and intracellular experimental results demonstrated a photothermal-enhanced CDT effect due to the increasing production of ROS at elevated temperature or upon laser treatment. The inhibitory effect of P@M on HepG2 cells further confirmed the efficacy of combined PTT/CDT treatment. These findings suggest potential for the design of tumor cell specifically activated PTT/CDT combined therapy based on POM-nanoplatforms.

Data availability

The data supporting this article have been included as part of the ESI.†

Author contributions

The manuscript was written through contributions of all authors. All authors have given approval to the final version of the manuscript.

Conflicts of interest

The authors declare no conflict of interest.

Acknowledgements

This research was supported by the Beijing Natural Science Foundation (2242015 and L233031), National Natural Science Foundation of China (22007004, 22178019, 22208013, 22288102, and 22207010) and the Fundamental Research Funds for the Central Universities (buctrc202010, XK1802-6, XK1803-05, and XK1902). All the experimental animals were humanely treated in accordance with the guidelines for animal care, and were approved by the Experimental Animal Welfare Ethics Committee of Beijing Institute of Technology.

References

1 D. An, J. Fu, B. Zhang, N. Xie, G. Nie, H. Ågren, M. Qiu and H. Zhang, NIR-II Responsive Inorganic 2D Nanomaterials for Cancer Photothermal Therapy: Recent Advances and Future Challenges, *Adv. Funct. Mater.*, 2021, **31**, 2101625.
2 Y. Li, M. Jiang, M. Yan, J. Ye, Y. Li, W. Dehaen and S. Yin, Near-infrared boron–dipyrrin (BODIPY) nanomaterials: Molecular design and anti-tumor therapeutics, *Coord. Chem. Rev.*, 2024, **506**, 215718.
3 S. G. Alamdari, M. Amini, N. Jalilzadeh, B. Baradaran, R. Mohammadzadeh, A. Mokhtarzadeh and F. Oroojalian, Recent advances in nanoparticle-based photothermal therapy for breast cancer, *J. Controlled Release*, 2022, **349**, 269–303.
4 S. Thirumurugan, S. Ramanathan, K. S. Muthiah, Y.-C. Lin, M. Hsiao, U. Dhawan, A.-N. Wang, W.-C. Liu, X. Liu, M.-Y. Liao and R.-J. Chung, Inorganic Nanoparticles for Photothermal Treatments of Cancer, *J. Mater. Chem. B*, 2024, **12**, 3569–3593.
5 X. Chen, J. S. Ponraj, D. Fan and H. Zhang, An overview of the optical properties and applications of black phosphorus, *Nanoscale*, 2020, **12**, 3513–3534.
6 F. Tang, A. Ding, Y. Xu, Y. Ye, L. Li, R. Xie and W. Huang, Gene and Photothermal Combination Therapy: Principle, Materials, and Amplified Anticancer Intervention, *Small*, 2023, **20**, 2307078.
7 J. Li, W. Zhang, W. Ji, J. Wang, N. Wang, W. Wu, Q. Wu, X. Hou, W. Hu and L. Li, Near infrared photothermal conversion materials: mechanism, preparation, and photothermal cancer therapy applications, *J. Mater. Chem. B*, 2021, **9**, 7909–7926.
8 H. S. Jung, P. Verwilst, A. Sharma, J. Shin, J. L. Sessler and J. S. Kim, Organic molecule-based photothermal agents: an expanding photothermal therapy universe, *Chem. Soc. Rev.*, 2018, **47**, 2280–2297.
9 C. Yin, X. Li, Y. Wang, Y. Liang, S. Zhou, P. Zhao, C. S. Lee, Q. Fan and W. Huang, Organic Semiconducting Macromolecular Dyes for NIR-II Photoacoustic Imaging and Photothermal Therapy, *Adv. Funct. Mater.*, 2021, **31**, 2104650.
10 J. Lu, L. Cai, Y. Dai, Y. Liu, F. Zuo, C. Ni, M. Shi and J. Li, Polydopamine-Based Nanoparticles for Photothermal Therapy/Chemotherapy and their Synergistic Therapy with Autophagy Inhibitor to Promote Antitumor Treatment, *Chem. Rec.*, 2021, **21**, 781–796.
11 H. Wang, K.-F. Xue, Y. Yang, H. Hu, J.-F. Xu and X. Zhang, In Situ Hypoxia-Induced Supramolecular Perylene Diimide Radical Anions in Tumors for Photothermal Therapy with Improved Specificity, *J. Am. Chem. Soc.*, 2022, **144**, 2360–2367.
12 J. Cheng, Y. Zhu, Y. Dai, L. Li, M. Zhang, D. Jin, M. Liu, J. Yu, W. Yu, D. Su, J. Zou, X. Chen and Y. Liu, Gas-Mediated Tumor Energy Remodeling for Sensitizing Mild Photothermal Therapy, *Angew. Chem., Int. Ed.*, 2023, **62**, e202304312.
13 X. Li, T. Yong, Z. Wei, N. Bie, X. Zhang, G. Zhan, J. Li, J. Qin, J. Yu, B. Zhang, L. Gan and X. Yang, Reversing insufficient photothermal therapy-induced tumor relapse and metastasis by regulating cancer-associated fibroblasts, *Nat. Commun.*, 2022, **13**, 2794–2812.
14 M. Zhang, H. Li, J. Zhang, H. Lv and G.-Y. Yang, Research advances of light-driven hydrogen evolution using polyoxometalate-based catalysts, *Chin. J. Catal.*, 2021, **42**, 855–871.

 This journal is © the Partner Organisations 2024

Published on 11 Khotavuxika 2024. Downloaded on 2026-02-17 05:35:50.

15 M. Aureliano, N. I. Gumerova, G. Sciortino, E. Garribba, A. Rompel and D. C. Crans, Polyoxovanadates with emerging biomedical activities, *Coord. Chem. Rev.*, 2021, **447**, 214143.
16 S. Lentink, D. E. Salazar Marcano, M. A. Moussawi and T. N. Parac-Vogt, Exploiting Interactions between Polyoxometalates and Proteins for Applications in (Bio) chemistry and Medicine, *Angew. Chem.*, 2023, **135**, e202303817.
17 L. Wang, P. Dai, H. Ma, T. Sun and J. Peng, Advancing biomedical applications of polyoxometalate-based metal–organic frameworks: from design to therapeutic potential, *Inorg. Chem. Front.*, 2024, **11**, 1339–1365.
18 J. Liu, M. Huang, X. Zhang, Z. Hua, Z. Feng, Y. Dong, T. Sun, X. Sun and C. Chen, Polyoxometalate nanomaterials for enhanced reactive oxygen species theranostics, *Coord. Chem. Rev.*, 2022, **472**, 214785.
19 B. Li, C. Xu, Y. Lv, G. Liu, X. Sun, Z. Sun, X. Xu, W. Chen, L. He and Y. F. Song, Vanadium-Substituted Polyoxometalates Regulate Prion Protein Fragment 106–126 Misfolding by an Oxidation Strategy, *ACS Appl. Mater. Interfaces*, 2023, **15**, 34497–34504.
20 C. Zhang, W. Bu, D. Ni, C. Zuo, C. Cheng, Q. Li, L. Zhang, Z. Wang and J. Shi, A Polyoxometalate Cluster Paradigm with Self-Adaptive Electronic Structure for Acidity/Reducibility-Specific Photothermal Conversion, *J. Am. Chem. Soc.*, 2016, **138**, 8156–8164.
21 G. Guedes, S. Wang, F. Fontana, P. Figueiredo, J. Lindén, A. Correia, R. J. B. Pinto, S. Hietala, F. L. Sousa and H. A. Santos, Dual-Crosslinked Dynamic Hydrogel Incorporating $\{Mo_{154}\}$ with pH and NIR Responsiveness for Chemo-Photothermal Therapy, *Adv. Mater.*, 2021, **33**, 2007761.
22 M. Tang, J. Ni, Z. Yue, T. Sun, C. Chen, X. Ma and L. Wang, Polyoxometalate-Nanozyme-Integrated Nanomotors (POMotors) for Self-Propulsion-Promoted Synergistic Photothermal-Catalytic Tumor Therapy, *Angew. Chem., Int. Ed.*, 2024, **63**, e202315031.
23 J. Mei, D. Xu, L. Wang, L. Kong, Q. Liu, Q. Li, X. Zhang, Z. Su, X. Hu, W. Zhu, M. Ye, J. Wang and C. Zhu, Biofilm Microenvironment-Responsive Self-Assembly Nanoreactors for All-Stage Biofilm Associated Infection through Bacterial Cuproptosis-like Death and Macrophage Re-Rousing, *Adv. Mater.*, 2023, **35**, 2303432.
24 Y. Shi, J. Zhang, H. Huang, C. Cao, J. Yin, W. Xu, W. Wang, X. Song, Y. Zhang and X. Dong, Fe-Doped Polyoxometalate as Acid-Aggregated Nanoplatform for NIR-II Photothermal-Enhanced Chemodynamic Therapy, *Adv. Healthcare Mater.*, 2020, **9**, 2000005.
25 H. Zhao, C. Zhao, Z. Liu, J. Yi, X. Liu, J. Ren and X. Qu, A Polyoxometalate-Based Pathologically Activated Assay for Efficient Bioorthogonal Catalytic Selective Therapy, *Angew. Chem., Int. Ed.*, 2023, **62**, e202303989.
26 L. W. C. Ho, Y. Liu, R. Han, Q. Bai and C. H. J. Choi, Nano-Cell Interactions of Non-Cationic Bionanomaterials, *Acc. Chem. Res.*, 2019, **52**, 1519–1530.
27 Z. Yue, J. Li, M. Tang, T. Sun, C. Chen and Z. Wu, Nanozyme-based Clusterphene for Enhanced Electrically Catalytic Cancer Therapy, *Adv. Healthcare Mater.*, 2024, **13**, 2303222.
28 T. Sun, W. Cui, M. Yan, G. Qin, W. Guo, H. Gu, S. Liu and Q. Wu, Target Delivery of a Novel Antitumor Organoplatinum(IV)-Substituted Polyoxometalate Complex for Safer and More Effective Colorectal Cancer Therapy In Vivo, *Adv. Mater.*, 2016, **28**, 7397–7404.
29 S. Zhou, F. Jia, Y. Wei, J. Du, J. Liu, W. Dong, J. Sui, W. Xue, Y. Yang, L. Chen, X. Meng and S. Yu, Metal–Organic Framework Nanocomposites in Conquering Hypoxia for Tumor Therapy, *Adv. Funct. Mater.*, 2024, **34**, 2314012.
30 R. Karimi Alavijeh and K. Akhbari, Cancer therapy by nano MIL-n series of metal-organic frameworks, *Coord. Chem. Rev.*, 2024, **503**, 215643.
31 X.-X. Li, D. Zhao and S.-T. Zheng, Recent advances in POM-organic frameworks and POM-organic polyhedra, *Coord. Chem. Rev.*, 2019, **397**, 220–240.
32 L. Guo, L. He, Q. Zhuang, B. Li, C. Wang, Y. Lv, J. Chu and Y. F. Song, Recent Advances in Confining Polyoxometalates and the Applications, *Small*, 2023, **19**, e2207315.
33 J.-N. Hao, K. Ge, G. Chen, B. Dai and Y. Li, Strategies to engineer various nanocarrier-based hybrid catalysts for enhanced chemodynamic cancer therapy, *Chem. Soc. Rev.*, 2023, **52**, 7707–7736.
34 Z. Lin, D. Liao, C. Jiang, A. Nezamzadeh-Ejhieh, M. Zheng, H. Yuan, J. Liu, H. Song and C. Lu, Current status and prospects of MIL-based MOF materials for biomedicine applications, *RSC Med. Chem.*, 2023, **14**, 1914–1933.
35 D. Cao, Q. Sha, J. Wang, J. Li, J. Ren, T. Shen, S. Bai, L. He and Y.-F. Song, Advanced Anode Materials for Sodium-Ion Batteries: Confining Polyoxometalates in Flexible Metal-Organic Frameworks by the "Breathing Effect", *ACS Appl. Mater. Interfaces*, 2022, **14**, 22186–22196.
36 C. Wu, D. Xu, M. Ge, J. Luo, L. Chen, Z. Chen, Y. You, Y.-x. Zhu, H. Lin and J. Shi, Blocking glutathione regeneration: Inorganic NADPH oxidase nanozyme catalyst potentiates tumoral ferroptosis, *Nano Today*, 2022, **46**, 101574.
37 L. Lai, W. Zou, Y. Zhang, Y. Tu, S. Li, T. Xin, T. Zhou, S. Xu, P. Zheng, Q. Pan and W. Zhu, Multifunctional MIL-101 nanoparticles with Fenton-like reactions to Co-deliver LL-37 peptide and Vancomycin for targeted NIR imaging and Drug-resistant bacteria treatment, *Chem. Eng. J.*, 2022, **435**, 135084.
38 H. Hu, H. Zhang, Y. Chen, Y. Chen, L. Zhuang and H. Ou, Enhanced photocatalysis degradation of organophosphorus flame retardant using MIL-101(Fe)/persulfate: Effect of irradiation wavelength and real water matrixes, *Chem. Eng. J.*, 2019, **368**, 273–284.
39 J.-C. Raabe, T. Esser, F. Jameel, M. Stein, J. Albert and M. J. Poller, Study on the incorporation of various elements into the Keggin lacunary-type phosphomolybdate

Published on 11 Khotavuxika 2024. Downloaded on 2026-02-17 05:35:50.

$[PMo_9O_{34}]^{9-}$ and subsequent purification of the polyoxometalates by nanofiltration, *Inorg. Chem. Front.*, 2023, **10**, 4854–4868.

40 Y. Murani, M. Memon, S. Singh and S. Pathan, Boosting the efficiency of supported undecamolybdophosphate catalyst by tailoring acid-redox properties for direct oxidative cross-esterification of aldehydes, *Chem. Eng. J.*, 2023, **478**, 147462.

41 Y. Jiang, Z. Wang, J. Huang, F. Yan, Y. Du, C. He, Y. Liu, G. Yao and B. Lai, A singlet oxygen dominated process through photocatalysis of CuS-modified MIL-101(Fe) assisted by peroxymonosulfate for efficient water disinfection, *Chem. Eng. J.*, 2022, **439**, 135788.

42 H. Zhang, D. Cui, T. Shen, T. He, D. Sun, S. An, B. Qi and Y.-F. Song, Engineering of PMo_{12}@NiCo-LDH composite via in situ encapsulation-reassembly strategy for highly selective photocatalytic reduction of CO_2 to CH_4, *Inorg. Chem. Front.*, 2023, **10**, 1421–1430.

43 G. Liu, J. Zhu, H. Guo, A. Sun, P. Chen, L. Xi, W. Huang, X. Song and X. Dong, Mo_2C-Derived Polyoxometalate for NIR-II Photoacoustic Imaging-Guided Chemodynamic/Photothermal Synergistic Therapy, *Angew. Chem., Int. Ed.*, 2019, **58**, 18641–18646.

44 D. Ni, D. Jiang, H. F. Valdovinos, E. B. Ehlerding, B. Yu, T. E. Barnhart, P. Huang and W. Cai, Bioresponsive Polyoxometalate Cluster for Redox-Activated Photoacoustic Imaging-Guided Photothermal Cancer Therapy, *Nano Lett.*, 2017, **17**, 3282–3289.

45 Z. Yang, W. Fan, W. Tang, Z. Shen, Y. Dai, J. Song, Z. Wang, Y. Liu, L. Lin, L. Shan, Y. Liu, O. Jacobson, P. Rong, W. Wang and X. Chen, Near-Infrared Semiconducting Polymer Brush and pH/GSH-Responsive Polyoxometalate Cluster Hybrid Platform for Enhanced Tumor-Specific Phototheranostics, *Angew. Chem., Int. Ed.*, 2018, **57**, 14101–14105.

46 Y. Li, W. Fan, X. Gu, S. Liu, T. He, S. Gou, W. Meng, M. Li, X. Liu, Y. Ren, C. Qi and K. Cai, Biodegradable Ferric Phosphate Nanocarriers with Tumor-Specific Activation and Glutathione Depletion for Tumor Self-Enhanced Ferroptosis and Chemotherapy, *Adv. Funct. Mater.*, 2024, **34**, 2313540.

47 H. Wang, D. Jiao, D. Feng, Q. Liu, Y. Huang, J. Hou, D. Ding and W. Zhang, Transformable Supramolecular Self-Assembled Peptides for Cascade Self-Enhanced Ferroptosis Primed Cancer Immunotherapy, *Adv. Mater.*, 2024, **36**, 2311733.

 This journal is © the Partner Organisations 2024